ABSTRACT

BHATTACHERJEE, UDITA. Experimental Study of Localizing an Aerial User and Application of Deep Neural Network in Localization. (Under the direction of Dr. Ismail Guvenc.)

The wireless industry is growing very fast in the last decade with the main aim of high-speed, low-latency, and reliable communication. Localization, being a primary and essential component of wireless communication, needs to be efficient enough to match modern requirements. With a higher range of frequency, not only the localization should be fast, but also it needs to be accurate. This thesis tries to address both these aspects of localization. In the first chapter, we discuss the improvement of localization accuracy for an aerial user. This is followed by the second chapter, where we discuss the benefits of using a deep neural network for faster and accurate localization utilizing a large number of historical databases that can be obtained in the current generation wireless networks.

In the first chapter, we localize aerial users in the form of unmanned aerial vehicles (UAVs). Unmanned aerial vehicles (UAVs) are being used for multiple purposes in the wireless industry e.g. military services, video surveillance, drone delivery. Extensive and uncontrolled use of UAVs may lead to privacy and security breaches. Hence, UAV monitoring is a hot research topic in the wireless industry. Tracking a UAV involves detecting and localizing it accurately. In the first part of this thesis, a UAV flying randomly in an open field is detected using a radio frequency (RF) sensor and localized using a commercially available Keysight Geolocation software N6854A. After evaluating the performance of the software localization algorithm against a groundtruth, the error is observed to be high occasionally. To improve the location accuracy, a popular bayesian filter named extended Kalman filter (EKF) is implemented over the location estimation of the localization algorithm. In state-of-art works, EKF is observed to perform well for a fixed motion model. In this research, the motion model is unknown and randomly changing. To counter that problem, the UAV trajectory is divided into small segments and fitted into either of three basic motion models: constant turn (CT), constant velocity (CV), and constant acceleration (CA). The result shows that the EKF can improve the location accuracy if the UAV trajectory points of a particular segment are aligned with the motion model definition of that segment.

The second half of the thesis explores the ways to escalate the localization process. There are multiple localization algorithms available in the literature. These algorithms are time and computationally efficient for the line of sight (LOS) communication. However, the algorithms become computationally heavy and time-consuming for non-LOS (NLOS) communication. In this part of the research, a deep neural network (DNN) is used to exploit the advantage of historical data from channel estimation. For a static environment, the previous channel estimation can be used to train a DNN for predicting the user location. Two different approaches are considered as the input of the DNN: the raw channel parameters and the channel response vector.

In the first approach, multiple combinations of channel parameters are chosen as the input to predict the location of the user. The result shows that the DNN can predict the location with great accuracy provided the DNN is trained in a supervised manner. In the second approach, the DNN fails to perform well due to the high correlation between the channels. The problem can be countered by representing the channel response in a sparse domain and then feeding it to the DNN. Overall, the use of DNN gives a promising result to achieve faster localization when the DNN is well trained.

Experimental Study of Localizing an Aerial User and Application of Deep Neural Network in Localization

by
Udita Bhattacherjee

A thesis submitted to the Graduate Faculty of
North Carolina State University
in partial fulfillment of the
requirements for the Degree of
Master of Science

Electrical Engineering

Raleigh, North Carolina

2021

APPROVED BY:

Dr. Mihail Sichitiu	Dr. Huaiyu Dai

Dr. Ismail Guvenc
Chair of Advisory Committee

DEDICATION

I dedicate my thesis to my parents, family, and friends for their support during my study and research.

BIOGRAPHY

The author was born in city-of-joy Kolkata, one of the metropolitan city in India (1995). She has completed her high school from the same city. In 2013, she joined her St. Thomas College of Engineering and Technology for her Bachelor's degree in Electronics and Communication Engineering. In 2017, she completed the degree and joined a start-up company Simplilearn solutions in Bangalore, India. After a few months in 2018, she joined a multinational company Cognizant Technology solutions as a Program analyst. After a journey of 1.5 years, she decided to pursue higher education and joined NC state university for Masters' degree in Electrical Engineering. The author worked on a small research problem during her Bachelors' final year and that motivated her for further research activity. From January 2020 she joined MPACT lab as a student worker as well as started her thesis research under Dr. Ismail Guvenc.

ACKNOWLEDGEMENTS

This thesis work was supported by NSF under the grant number CNS-1814727, INL Laboratory Directed Research & Development (LDRD) Program under DOE Idaho Operations Office Contract DE-AC07-05ID14517, and NSF PAWR program under grant number CNS-1939334. Firstly, I would like to thank both the projects for supporting the expense of publishing the work and spreading my work to a larger community. Secondly, I am grateful to my thesis advisor Dr. Ismail Guvenc for his continuous support and guidance to help to be a better researcher. Also, I thank my two committee members Dr. Mihail Sichitiu and Dr. Huaiyu Dai for their valuable feedback and inputs. I would also like to thank all my co-authors Dr. Ender Ozturk, Dr. Ozgur Ozdemir, Chethan Kumar Anjinappa, and LoyCurtis Smith for their help in making the publication happen.

TABLE OF CONTENTS

LIST OF TABLES

LIST OF FIGURES

Chapter 1

INTRODUCTION

The amount of data for transmission is rapidly increasing with the advancement of life. Hence, the wireless industry is now implementing 5G and working towards 6G to fulfill the need for high-speed, low-latency, and reliable data communication wirelessly. With the usage of high-frequency bands in 5G and upcoming technologies, researchers are facing multiple environmental issues like high scattering, path loss, the effect of weather, etc. Researchers are working on handling these issues using beaming forming techniques, implementing the multiple-input-multiple-output (MIMO) system, increasing the number of transmitters, etc. Localization, the process of determining the location of a user is one of the essential components for successful communication some of the use cases being beamforming, location-based services, and remote area coverage. With a higher range of frequency, not only the localization should be fast, but also it needs to be accurate. This thesis tries to address both these aspects of localization. In the first chapter, we discuss the improvement of localization accuracy for an aerial user. This is followed by the second chapter, where we discuss the benefits of using a deep neural network for faster and accurate localization utilizing a large number of historical databases that can be obtained in the current generation wireless networks.

1.1 Layout and Contributions

1.1.1 Chapter 2

In the modern era of telecommunication, higher frequency bands are used which results in high path loss. Hence, industry and academia are considering all the possible ways of communication to counter the path loss effect. Unmanned aerial vehicles (UAVs) are used for aerial communication in different areas like drone delivery, video surveillance, small area coverage, etc. However, the extensive use of UAV is raising privacy and security issues presently. Detecting and tracking a UAV is becoming an essential step to avoid any security breach. Chapter 2 of this thesis talk through an experimental study which is conducted to detect and localize a UAV flying in an open field. A UAV can be detected using different types of equipment e.g. passive radio fre-

quency (RF) radar, multiple-input-multiple-output (MIMO) radar, optical and acoustic radars. In this case, a commercially available RF sensor (Keysight RF sensor N6841A) is used to detect the UAV in the field. After successfully detecting the flying UAV, Keysight geolocation software N6854A is used to localize the UAV and the localization performance is evaluated against a ground-truth value. The performance is observed to be bad for some of the measurement points. To improve the location accuracy a popular bayesian filter technique named extended Kalman filter (EKF) is adopted. EKF is famous for tracking automated vehicles and UAVs. In state-of-art works, people define a fixed system model for the automated vehicle or UAV which helps the EKF to improve the location error. But it is hard to know the exact system model for a randomly flying UAV which is the target for this research. This work shows that the EKF can still be applied to improve the location accuracy by segmenting the trajectory in small parts. After segmentation, each segment is fitted to either of three basic system models: constant turn (CT), constant velocity (CV), constant acceleration (CA). Hence, each segment has a fixed motion model and an usual EKF algorithm can be applied to improve the location accuracy. The details of the segmentation and results are shown in Chapter 2.

1.1.2 Chapter 3

As a part of localization, the network has to perform channel estimation for each user at every location. In a fixed environment, the historical channel estimation data can be used to train a deep neural network (DNN) for future localization. Following this idea in the chapter 3 of the thesis, a DNN has been designed for a static environment to predict the user location for both LOS and NLOS paths. Once the DNN is trained, it can predict the location real-time with very low complexity. But the problem is how to train the DNN well enough to achieve a good performance. Two approaches are considered for this work: one using raw channel parameters, and the other one using the channel response vector as the input of the DNN. In both the case, the DNN is supposed to predict the x and y coordinate of the user as output. In the first approach, multiple combinations of the angle of arrival (AoA), received signal strength (RSS), and time of arrival (ToA) is used as input of the DNN keeping the number of multipath components fixed. In reality, the number of multipath components above a threshold signal strength varies from point to point. Hence, the second approach uses the channel response vector as DNN input since it is independent of the number of multipath components. The learning is performed in a supervised manner for two different frequencies: 5 GHz and 28 GHz. The details of the research and the comparison of the results are discussed in Chapter 3.

Chapter 2

Experimental Study of Outdoor UAV Localization and Tracking using Passive RF sensing

Research Outcome

- **U. Bhattacherjee**, E. Ozturk, O. Ozdemir, I. Guvenc, M. L. Sichitiu, and H. Dai "Experimental Study of Outdoor UAV Localization and Tracking using Passive RF sensing," [Submitted to ACM WiNTECH 2021].

2.1 Summary of the Chapter

Extensive use of unmanned aerial vehicles (UAVs) is expected to raise privacy and security concerns among individuals and communities. In this context, detection and localization of UAVs will be critical for maintaining a safe and secure airspace in the future. In this chapter, Keysight N6854A radio frequency (RF) sensors are used to detect and locate a UAV by passively monitoring the signals emitted from the UAV. First, Keysight sensor detects the UAV by comparing the received RF signature with various other UAVs' RF signatures in Keysight database using an envelope detection algorithm. Afterwards, time difference of arrival (TDoA) based localization is performed by a central controller using the sensor data, and the drone is localized with some error. To mitigate the localization error, implementing an extended Kalman filter (EKF) is proposed in this research. Performance of the proposed approach is evaluated on a realistic experimental dataset. EKF requires basic assumptions on the type of motion throughout the trajectory, i.e., the movement of the object is assumed to fit some motion model (MM) such as constant velocity (CV), constant acceleration (CA), and constant turn (CT). In the experiments, an arbitrary trajectory is followed, therefore it is not feasible to fit the whole trajectory into a single MM. Consequently, the trajectory is segmented into sub-parts and

a different MM is assumed in each segment while building the EKF model. Simulation results demonstrate an improvement in error statistics when EKF is used if the MM assumption aligns with the real motion.

2.2 Introduction

Unmanned aerial vehicles (UAVs), commonly known as drones, are expected to be an important component in next-generation wireless systems [1]. UAVs have multiple commercial, government, and personal uses, ranging from goods delivery, live video surveillance, photography, among others. On the other hand, UAVs can also be used to breach public privacy and security, and sometimes UAV swarms may threaten sensitive facilities such as nuclear plants, oil installations, and large public gatherings. Thus, detecting, locating, and tracking UAVs is of great importance. A few popular techniques for UAV detection include the use of optical or acoustic radars [2, 3], passive radio frequency (RF) radars [4], and MIMO radars [5]. These detection techniques have their distinct advantages/disadvantages, and are chosen based on the need and type of a specific application, UAV size under consideration, among other criteria. For instance, small UAVs are harder to detect by radars as their radar cross-section (RCS) is similar to a bird [6] and their acoustic signature is typically weak to be detected by acoustic radars [7]. A popular and effective approach to UAV detection is passive RF sensing of UAV and controller signals [8, 9], which is the focus of our work.

Majority of the UAVs use 2.4 GHz and 5.8 GHz ISM (Industrial Scientific and Medical) frequency bands to communicate with the remote controllers. Therefore, an RF sensor can passively detect and localize the UAVs using the RF signals. In this chapter, we detect the RF signals and localize UAVs using the Keysight Geo location system N6854A with the data collected by RF sensor N6841A. The sensor is capable of detecting RF sources in the vicinity of 1-2 km in sub-6 GHz bands, and inter-operates with a geolocation tool, N6854A [10], which performs localization. Occasionally these RF sensors may perform poorly resulting in large localization errors as in [11], where the authors utilized an N6841A sensor in a spectrum sensing module. These high errors are not acceptable for some critical applications. In this context, we propose an extended Kalman filter (EKF) framework in this chapter to improve tracking accuracy for GPS-denied environments.

The accuracy of the EKF algorithm relies on the dynamics of the UAV trajectory. One way of modeling the problem of localizing a highly maneuvering UAV with an unknown pattern is to segmentize the trajectory and use multiple motion models (MMs) that represent the possible maneuvering patterns for each segment [12]. This approach assumes that the UAV follows one of the possible models and the precision of the model depends on the accuracy of this assumption. In this chapter, a multiple MM-based EKF framework is adopted that considers three types of motion, i.e., moving in a circular trajectory and moving on a straight line with constant velocity or constant acceleration. More specifically, these three kinematic models are labelled as

constant turn (CT), constant velocity (CV), and constant acceleration (CA) models. A multi-MM framework models the trajectory better and, thus, provide better performance than a single-MM model.

The core purpose of this study is to analyze the performance of the EKF-based tracking with different MMs and its relationship to parameter selection (e.g., noise covariance) on a realistic dataset. The rest of the chapter is organized as follows. Section 2.3 presents the measurement setup, details of the Keysight geolocation system, the UAV trajectory, and the results after post-processing the data. The EKF implementation along with the modeling of multiple MM are presented in Section 2.4. The numerical results along with insights and discussions are given in Section 2.5.

2.3 Experiment Setup and Measurements

This section briefly describes the capabilities and data collected by the RF sensors along with its important parameter selection (e.g., noise covariance). This is followed by the presentation of UAV trajectory in an open field and the simulation results from the N6854A system for the post-processed data.

2.3.1 RF Sensor System and the UAV

In this chapter, commercially available Keysight RF sensor N6841A[1] is used for detecting, recording, and time-stamping the UAV downlink RF signals. The sensor node consists of RF sensor N6841A, a GPS antenna, and a broadband antenna as shown in Fig. 2.1a. The RF receiver operates in the frequency range of 20 MHz - 6 GHz and has a bandwidth up to 20 MHz. The broadband antenna is omnidirectional for better reception, and the GPS antenna helps to record the timestamps of the RF sensor collected data. This sensor system is also accompanied by a localization software called *geolocation software N6854A* [10] that can localize RF sources within a 2 km radius.

The geolocation software is capable of calculating time-frequency response, correlation amongst the RF sensors, and localization. For localization task, it offers three different algorithms, i.e., the time-difference-of-arrival (TDoA) based, the received-signal-strength (RSS) based, and a hybrid algorithm of the former two. The performance of these algorithms depends on the scattering environment. For instance, TDoA-based localization is preferred over RSS-based localization when the number of multipath components (MPCs) is low [14]. In a rich-scattering environment, the TDoA-based algorithm performs poorly, so the RSS-based algorithm is preferred. This experiment was conducted in a large open field with a dominant line-of-sight (LOS) path and very weak reflections, hence, TDoA-based localization approach was preferred. Furthermore, a commercially available drone, a DJI Inspire 2, operating at 2.400

[1]These RF sensors are also being deployed as a part of the *AERPAW: Aerial Experimentation and Research Platform for Advanced Wireless* [13], a large-scale 5G testbed focused on wireless communications and UAVs.

(a) (b)

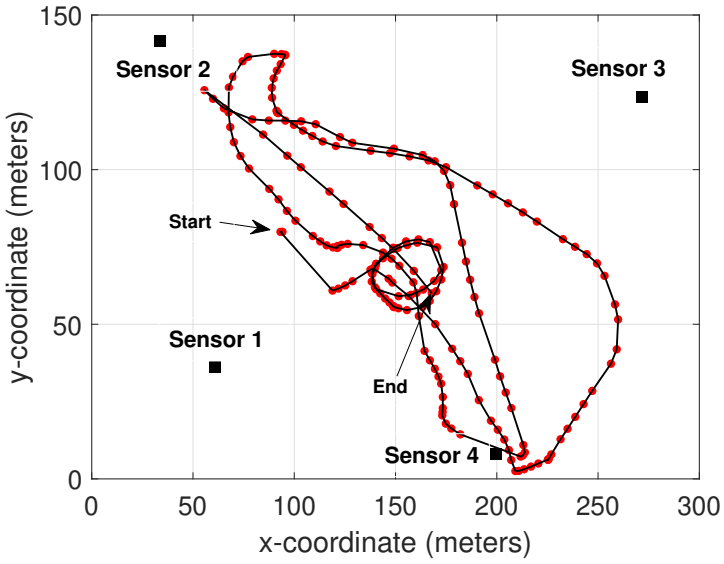

(c)

Figure 2.1 (a) Keysight RF sensor N6841A. b) Google Earth snapshot of Dorothea Dix park and location of the sensors. (c) Experimental UAV trajectory relative to the sensor locations.

- 2.483 GHz band with a bandwidth of 20 MHz was used as the target that is controlled with an RF remote controller.

2.3.2 RF Sensor Measurement Setup and UAV Trajectory

The experiment with Keysight RF sensors and the UAV was conducted in Dorothea Dix Park, Raleigh, North Carolina. The experiment field is shown in Fig. 2.1b, where white boxes are

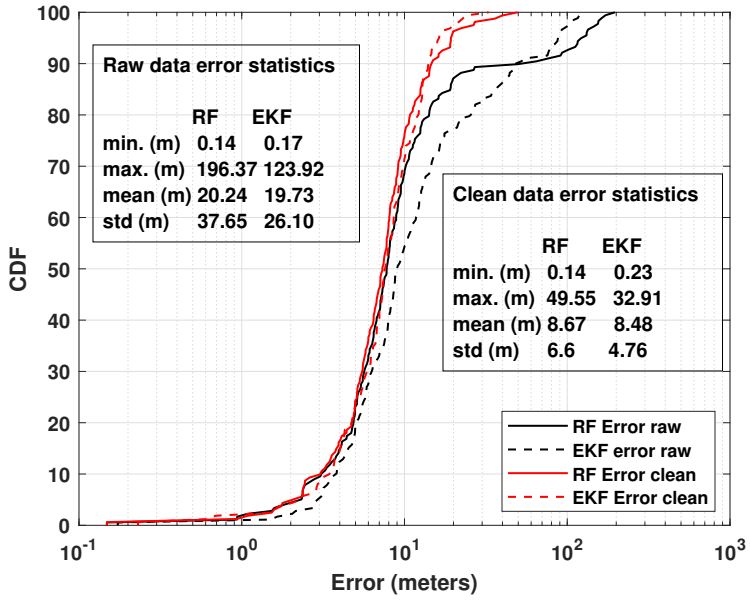

Figure 2.2 Error CDF of the raw and clean data from the RF sensor and EKF against ground truth locations.

the RF sensors' location (black square points in Fig. 2.1c). In total, four Keysight N6841A RF sensors were used to localize a UAV, and these sensors had a separation distance of at least 50 meters. For the system functionality, at least one of the RF sensors should be connected with a PC to monitor the UAV RF signals. These sensors can also be accessed via the internet. Each of the RF sensors collects the RF signals' in-phase and quadrature (IQ) data. The collected data is post-processed by the geolocation software to estimate the UAV location using the TDoA-based algorithm. Upon performing localization, the geolocation software provides the latitude and longitude of the UAV in decimal degrees and does not provide the altitude information. Location estimates are logged in conjunction with their respective timestamps.

The UAV trajectory in the experiment based on the location data collected by the drone is shown in Fig. 2.1c in 2-D. Apparent from the figure that the UAV was flown arbitrarily given the start and end point of the trajectory as pointed in the Fig. 2.1c. It is explicit that such a trajectory cannot be modeled with a single MM (e.g., CV or CT) for the EKF framework to perform good. More details on the approximation of the trajectory are discussed in Section 2.4. Further, during the flight, the UAV records its location and saves it (with the timestamps) in every 100 msec. This location information is used as the ground truth to evaluate the performance of the RF sensor system and the proposed EKF approach. Up next, the further data processing on the collected experimental data is discussed.

2.3.3 Data Post-processing and RF Sensor Error Performance

With the experimental setup mentioned above, the UAV location data and the estimated locations from the RF sensor paired with corresponding timestamps were collected for around 5 minutes of flight time. The collected location information from both the UAV and RF sensors was converted from decimal degrees into cartesian coordinates for ease of representation. Further, the sampling time intervals of the UAV and RF sensor data are not equal[2]. So to be able to work on a consistent dataset, two datasets were compared and a few samples were filtered out for which the timestamps do not match in millisecond sensitivity. After this process, a total of $K = 178$ discrete timestamps are considered for further processing. The processed UAV and RF sensor locations at k^{th} time index are denoted by $\mathbf{l}_k^{\text{UAV}}$ and $\mathbf{l}_k^{\text{RF}}$, respectively. These data points are used for evaluating the performance of the geolocation system.

The performance of the geolocation system is evaluated using the Euclidean distance metric. The black solid curve in Fig. 2.2 shows the cumulative distribution function (CDF) plot of the error between the RF sensor estimations and the UAV GPS data. The error statistics (e.g., max, min, mean, and std) are also calculated for the processed data points. Occasionally, the estimated location is far away from the true points corresponding to a higher error in the upper tail of the CDF (maximum of 198.4477 m). A possible explanation for this phenomenon is that the RF sensors would have intermittently detected other RF signal sources in a 1-2 km radius resulting in erroneous estimation. To disregard these erroneous data points, the data was cleaned by removing the points with an error higher than 60m. The resulting data points are referred as *clean data*, whereas the data set with all the points are referred *raw data*. The solid red curve in Fig. 2.2 shows the error CDF of the clean data. The highest error on this curve is around 50 m and the errors are greater than 14 m 90% of the time. This much error might be too high depending on the application. The accuracy of the sensors can be improved by the use of an EKF framework, especially for the high error portions of the CDF plot.

2.4 Motion Model based EKF

This section first gives details of the proposed EKF approach for a discrete-time system followed by the working principle of the MMs and segmentation of the trajectory.

2.4.1 EKF Tracking Framework

The primary objective of discrete EKF tracking is to estimate the present state given the information of the previous states in terms of time. Target tracking methods are usually model-based and are expressed in terms of the target dynamic MM and its observation model, respectively.

[2]The number of data points from the RF sensors (sampling rate $\sim$ 1 sample/sec) is lower than the number of data points at the UAV (sampling rate $\sim$ 1 sample/100msec).

Mathematically, a discrete-time model is expressed as follows [15]

$$\begin{aligned} \textbf{State model:} \quad & \mathbf{s}_k = f_k(\mathbf{s}_{k-1}, u_k) + \mathbf{w}_{k-1}, \\ \textbf{Observation model:} \quad & \mathbf{z}_k = \mathbf{H}\mathbf{s}_k + \mathbf{v}_k, \end{aligned} \tag{2.1}$$

where, k denotes the state (time) index $k \in \{1, \ldots, K\}$. In the state model, the term $\mathbf{s}$ denotes the state vector which consists of the parameters for predicting in each state. This representation of state is core to the EKF process and is basically the minimum information required about the past and present to determine the future response given the future input. The function f_k is the vector-valued (time-varying) function that dictates the state transition. In the observation model, $\mathbf{z}_k$ and $\mathbf{H}$ denote the observations at the state index k and observation matrix (not a time-varying function in this work as the position estimates are obtained only from the RF sensor), respectively. Finally, the terms $\mathbf{w}_k$ and $\mathbf{v}_k$ are the process and observation noises that take into account any irrelevant attribute affecting the state and observations. Both $\mathbf{w}_k$ and $\mathbf{v}_k$ are assumed to be zero-mean Gaussian distribution with the covariances $\mathbf{Q}_k$ and $\mathbf{R}_k$ that control the level of relaxation of the constant-term MM assumptions and measurement noise level, respectively. Importantly, the choice of the state components $\mathbf{s}_k$, the function f_k that accounts for the effect of target motion, and the covariance matrix $\mathbf{Q}_k$ depends on the choice of the motion-model (MM).

2.4.2 Kinematic Motion Models (MMs)

To better model the random trajectory of the UAV, three tractable kinematic models are used, namely, constant velocity MM (CV-MM), constant acceleration MM (CA-MM), and constant turn MM (CT-MM). The trajectory will be segmentized and only one of these MMs will be used for a single segment. Note that, unlike many other works in the literature, arbitrariness of our trajectory makes it impossible to model the whole trajectory with a single MM. The three considered MMs are described below. Readers can refer to [15] for further details.

1) CV-MM: The simplest form of motion is the CV-MM, where the speed and the direction of the object is constant, i.e., the object moves in a straight line. For this MM, the minimum information required in the state model to capture the future response are the current positions and the velocity. This is represented by $\mathbf{s}_k$. The state vector and discrete-time linear state transition matrix, f_k in (2.1) are as follows [15, Equation (16)]

$$\mathbf{s}_k^{\mathrm{CV}} = \begin{bmatrix} x \\ y \\ \dot{x} \\ \dot{y} \end{bmatrix}, \quad \mathbf{f}_k^{\mathrm{CV}} = \begin{bmatrix} 1 & 0 & T_k & 0 \\ 0 & 1 & 0 & T_k \\ 0 & 0 & 1 & 0 \\ 0 & 0 & 0 & 1 \end{bmatrix},$$

where the terms $\dot{x}$, $\dot{y}$, T_k denote the velocity in x and y directions, and interval between the time-indices $k-1$ and k, respectively.

2) CA-MM: The second considered MM is the CA-MM that has constant acceleration where the velocity is changing with a constant rate each second and is captured in the state vector by the terms $\ddot{x}$ and $\ddot{y}$ denoting the acceleration in x and y directions, respectively. The state vector and discrete-time linear state transition matrix, f_k in (2.1) are as follows [15, Equation (21)]

$$\mathbf{s}_k^{\mathrm{CA}} = \begin{bmatrix} x \\ y \\ \dot{x} \\ \dot{y} \\ \ddot{x} \\ \ddot{y} \end{bmatrix}, \quad \mathbf{f}_k^{\mathrm{CA}} = \begin{bmatrix} 1 & 0 & T_k & 0 & \frac{T_k^2}{2} & 0 \\ 0 & 1 & 0 & T_k & 0 & \frac{T_k^2}{2} \\ 0 & 0 & 1 & 0 & T_k & 0 \\ 0 & 0 & 0 & 1 & 0 & T_k \\ 0 & 0 & 0 & 0 & 1 & 0 \\ 0 & 0 & 0 & 0 & 0 & 1 \end{bmatrix}.$$

3) CT-MM: This MM captures the object moving in a circular path with a constant angular velocity of ω (rad/sec). The state-space equations expressed in Cartesian [16] are as follows:

$$\mathbf{s}_k^{\mathrm{CT}} = \begin{bmatrix} x \\ y \\ \dot{x} \\ \dot{y} \\ \phi \end{bmatrix}, \mathbf{f}_k^{\mathrm{CT}}(\mathbf{s}_k) = \begin{bmatrix} x + \frac{\dot{x}}{\omega}\sin(\omega T_k) - \frac{\dot{y}}{\omega}(1 - \cos(\omega T_k)) \\ \dot{x}\cos(\omega T_k) - \dot{y}\sin(\omega T_k) \\ y + \frac{\dot{x}}{\omega}(1 - \cos(\omega T_k)) + \frac{\dot{y}}{\omega}\sin(\omega T_k) \\ \dot{x}\sin(\omega T_k) + \dot{y}\cos(\omega T_k) \\ \omega \end{bmatrix}.$$

Regarding the noise factors, this study assumes that the process noise,$\mathbf{w}_k$, is uncorrelated across its components, and adopts the covariance structure $\mathbf{Q}_k$ as explained in [15, Equation (17, 22)].

On the other hand, only the position information is available from the RF sensor for the measurement noise, $\mathbf{v}_k$, and this is reflected by the measurement model for each of the MMs as follows

$$\mathbf{H}^{\mathrm{CV}} = \begin{bmatrix} 1 & 0 & 0 & 0 \\ 0 & 1 & 0 & 0 \end{bmatrix}, \quad \mathbf{H}^{\mathrm{CA}} = \begin{bmatrix} 1 & 0 & 0 & 0 & 0 & 0 \\ 0 & 1 & 0 & 0 & 0 & 0 \end{bmatrix},$$
$$\mathbf{H}^{\mathrm{CT}} = \begin{bmatrix} 1 & 0 & 0 & 0 & 0 \\ 0 & 1 & 0 & 0 & 0 \end{bmatrix}.$$

Apart from the above-mentioned models, one might also consider other sophisticated MMs [17] such as constant jerk, simultaneous deceleration, and turn, oscillatory turns, etc. However, only these three models are used in this case as these three models are sufficient to model the whole trajectory. The crucial part of the process is to decide how to do the segmentation of the trajectory and assigning an MM for each segment. In practice, this can be achieved using some data-driven estimators [18], camera-based you-look-only-once (YOLO) detection methods [19],

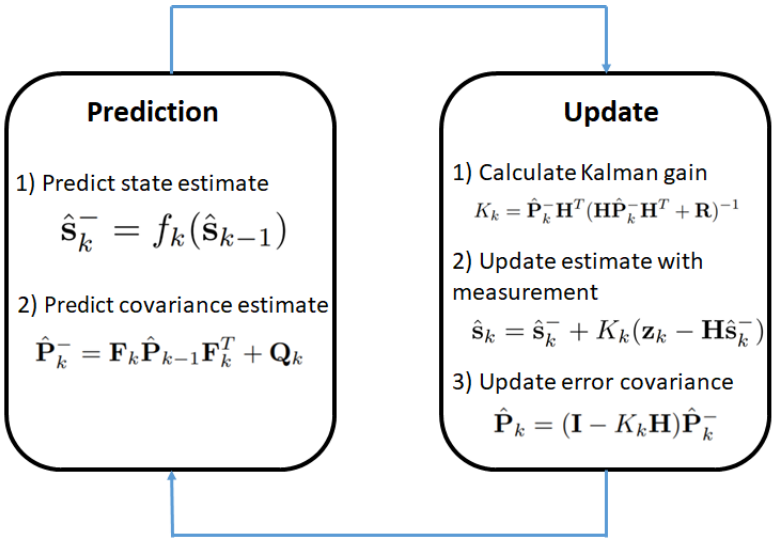

Figure 2.3 EKF steps for each time index k.

or leveraging environmental priors (physical constraints and environmental semantics) and motion history. However, for the sake of simplicity and tractability, it is assumed that the segments and which MMs to be used is perfectly known apriori.

2.4.3 Implementation of EKF

In this subsection, the details of the implementation of the EKF is discussed. The flow diagram is given in Fig. 2.3. An EKF process is comprised of two consecutive steps, i.e., the prediction step and the update step.

In the prediction step, the target state $\hat{\mathbf{s}}_k$ and the covariance $\hat{\mathbf{P}}_k^-$ at time index k are predicted based on the kinematic process MMs, previous state $\hat{\mathbf{s}}_{k-1}$, and covariance estimate. These predictions will further be used in the update step, where the EKF updates the predicted state based on the Kalman gain K_k and the measurement $\mathbf{z}_k$. The Kalman gain K_k acts as a weighting factor that signifies the trustable value of the measurement and prediction state values. If the observations are assumed to be highly noisy (high variance), then K_k will be low weighing less on the measurements and more on the predicted values, and vice-versa. Readers can refer to [20] for further details. The above process is recursive and repeated for each time index k. All the implementation were carried out using the *trackingEKF* built-in function of the *Sensor Fusion and Tracking Toolbox* of Matlab®.

2.5 Experiment Results and Discussion

In this section, the performances of different MMs are observed on a realistic maneuvering UAV target. The statistics of the Euclidean distance metric $d_k(\mathbf{l}_k^{\text{UAV}}, \mathbf{l}_k^{\text{Est.}}) = ||\mathbf{l}_k^{\text{UAV}} - \hat{\mathbf{l}}_k^{\text{Est.}}||_2$ is used

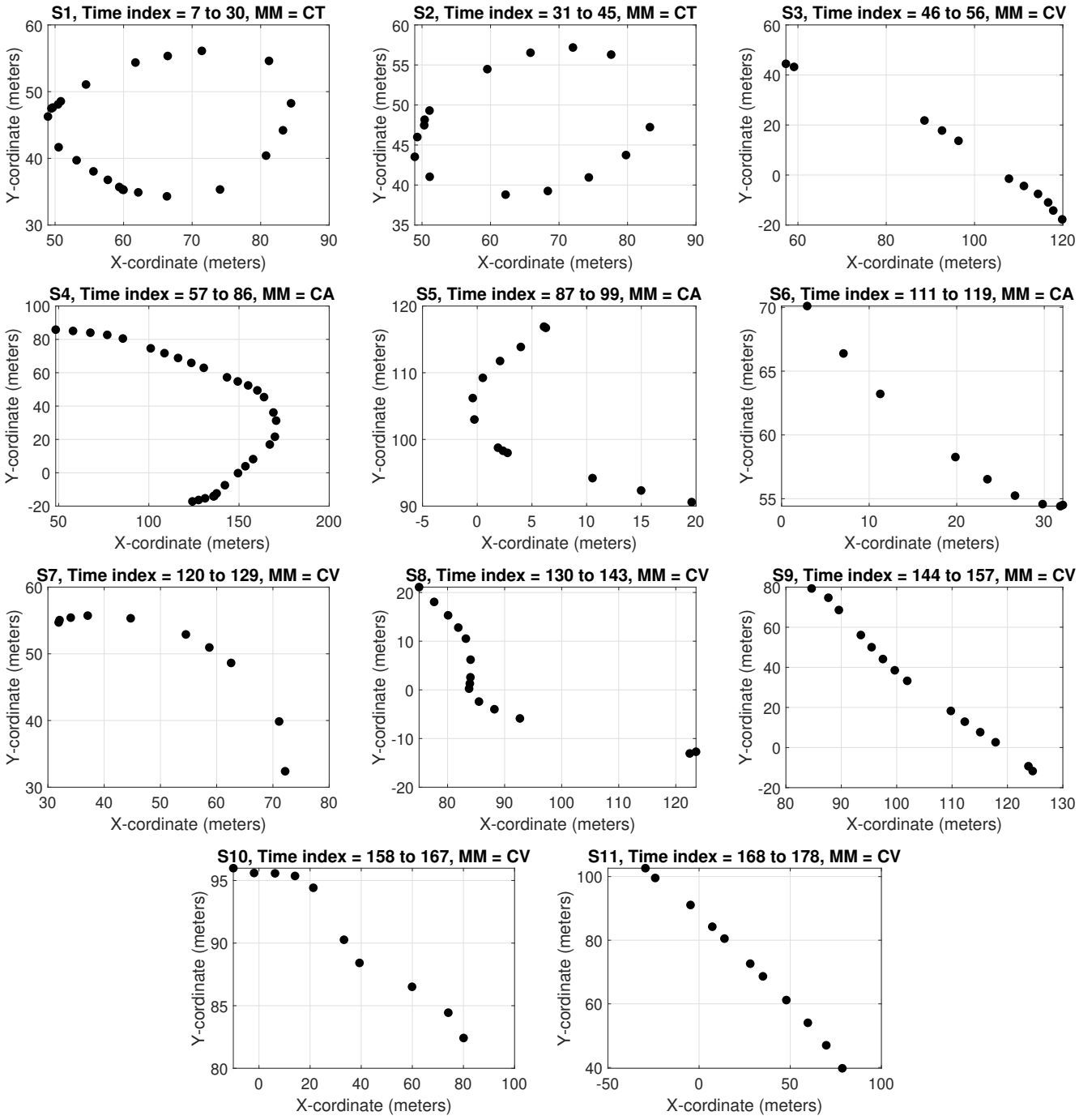

Figure 2.4 Segmentation of the complete UAV trajectory into appropriate MMs.

to evaluate the performance of both RF sensors and EKF. The terms $\hat{\mathbf{l}}_k^{\mathrm{UAV}}$ and $\hat{\mathbf{l}}_k^{\mathrm{Est.}}$ denote the ground truth (UAV GPS) and estimated locations (RF and EKF algorithms), respectively.

2.5.1 UAV Trajectory and Segmentation

The UAV trajectory flown for the experiment is as shown in Fig. 2.1c with the red points being the measurement points and black line connecting the points with straight line. As noted in Section 2.3, after post-processing, a total of $K = 178$ discrete time-stamps for the considered trajectory has been used for EKF implementation. First, the complete trajectory is divided manually into segments based on the visual inspection of the trajectory and velocity information obtained from the UAV, both are illustrated in Fig. 2.4 and Fig. 2.5. The trajectory knowledge and velocity variations within the segment would be sufficient to approximate a segment as either of the MMs [21]. Fig. 2.4 shows the segmentation of the complete trajectory into eleven different stages of maneuvering along with its corresponding time indices and approximated MMs. Fig. 2.5 shows the total velocity plot of the UAV trajectory for the complete trajectory according to the GPS data collected by the UAV. For ease of illustration, the CT, CA, and CV MMs are colored red, green, and yellow, respectively. These two figures complement each other and justify the segmentation. Initial UAV take off and an interim part of the trajectory with many missing data points are colored white in Fig. 2.5 indicating that these segments are excluded.

Considering both Fig. 2.4 and Fig. 2.5, first two segments (S1-S2) are approximated with CT-MM, and similarly, CA-MM is used for the segments S4, S5 and S7. The remaining segments, S3, S6, S8, S9, S10, and S11, are approximated as CV-MM due to approximated straight lines and velocities. Even though CV-MM is the best choice for this third segment group, EKF accuracy will reduce because of the deviation from idealized MM assumption due to high variations in velocity. The mean and standard deviation of velocity for CV and CT segments and those of acceleration for CA segments are also shown in Fig. 2.5.

2.5.2 EKF Parameters Selection Strategy

While building the EKF model for each segment, the initial point was chosen to be the location measured by the RF sensor system. These estimates are noisy and the noise level is characterized by a covariance matrix $\mathbf{R}_k = diag\{\sigma_x^2, \sigma_y^2\}$, where σ_x^2 and σ_y^2 values are chosen as the mean of the RF sensor location error. On the other hand, the process noise covariance matrix elements depend on the MM and are treated as design parameters. These elements are the velocity variance $\sigma_{\dot{x}}^2$ and $\sigma_{\dot{y}}^2$, acceleration variance $\sigma_{\ddot{x}}^2$ and $\sigma_{\ddot{y}}^2$, and variance of turn-rate σ_ω^2. These parameters have been kept fixed for each segment using the variance of the respective domain segments obtained from the UAV data.

2.5.3 Performance Analysis

EKF is applied separately to each segment and the error performances are studied of the RF sensor and the proposed tracking EKF algorithms . The error CDF curves for both *raw data* and *clean data* are also given in Fig. 2.2. The black and red solid lines represent the error of

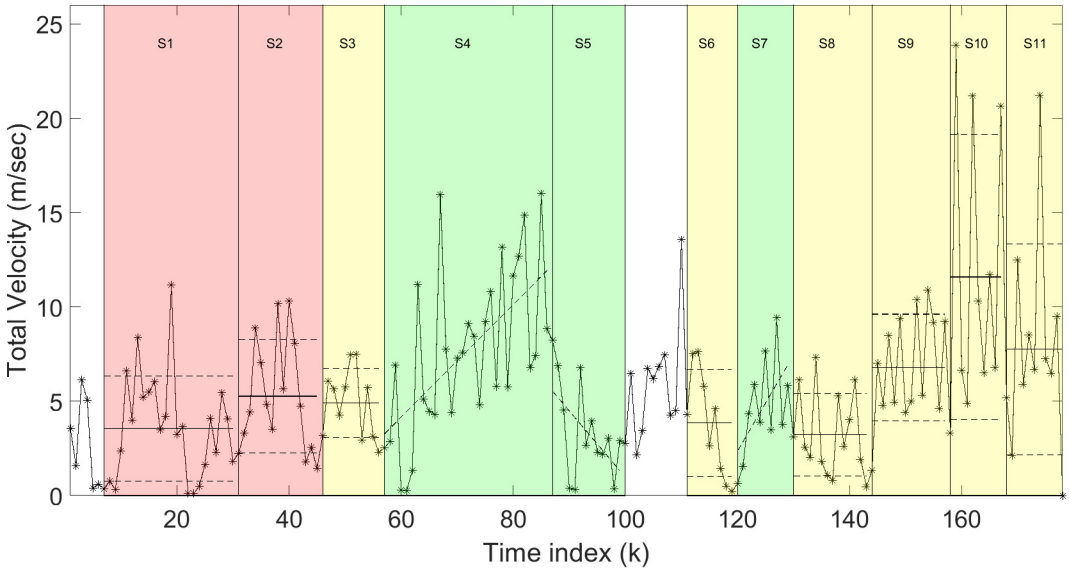

Figure 2.5 Total velocity plot for clean UAV trajectory data where S1 - S2: CT, S4, S5, S7: CA, S3, S6, S8 - S11: CV

Table 2.1 Error statistics for each segment (Clean data, Error < 60 m).

	S1		**S2**		**S3**		**S4**		**S5**		**S6**	
Err. stats.	**RF**	**EKF**	**RF**	**EKF**	**RF**	**EKF**	**RF**	**EKF**	**RF**	**EKF**	**RF**	**EKF**
min. (m)	1.08	**0.23**	0.93	**0.35**	5.3	5.65	0.14	4.2	5.54	7.4	1.53	**0.68**
max. (m)	14.25	**13.88**	9.04	9.73	15	14.84	39.89	**19.89**	49.55	**32.91**	7.32	**7.3**
mean (m)	7.7	8.0	5.89	6.39	8.89	8.97	10.59	**9.67**	14.63	**13.84**	4.72	**4.7**
std (m)	3.64	**3.49**	2.28	2.59	3.23	**2.79**	7.7	**3.8**	11.87	**6.89**	2.13	2.49

the *raw data* and *clean data*, whereas, the dashed black and red lines are the error CDFs of the EKF predicted data. As expected, the results are better for the *clean data* since EKF can reduce the highest error without disrupting errors of the rest much. On the other hand, the highest error is reduced significantly for the *raw data* with the cost of an increase in errors of the remaining points. This is because the noise varies highly from point to point for some segments, and it is hard for EKF to perform well for all the points with fixed noise covariance. For the error analysis in each segment, this study focus only on the *clean data* and compare the maximum, minimum, mean, and standard deviation (std) of calculated errors, and highlight the lowest error. These values are listed Table 2.1, and 2.2.

For both CT-MM segments (S1 and S2), the maximum error with the EKF is reduced significantly compared to the RF sensor even if it does not take into account the dynamic modeling. Thus, even an approximated MM-based EKF can help to reduce the highest error significantly. The EKF even helps reduce the minimum and std error for S1. For S2, the results are not improved but rather increased. This might be due to the nonalignment of the points with the circular assumption and velocity variation. Note that CT-MM assumes a constant

Table 2.2 Error statistics for each segment (Clean data, Error < 60 m).

	S7		S8		S9		S10		S11	
Err. stats.	**RF**	**EKF**	**RF**	**EKF**	**RF**	**EKF**	**RF**	**EKF**	**RF**	**EKF**
min. (m)	2.33	**1.69**	2.39	**1.41**	6.46	**3.17**	1.75	2.28	2.04	**2.02**
max. (m)	35.81	**23.86**	14.67	14.67	27	**19.53**	17.06	**12.84**	16.17	16.31
mean (m)	7.68	**5.81**	5.99	6.54	10.72	**10.3**	8.23	**7.02**	7.36	7.52
std (m)	9.94	**6.46**	3.97	4.13	5.66	**4.24**	4.96	**3.37**	5.1	5.15

angular velocity. A similar trend can be noticed for CA-MM and CV-MM segments. Among all the CA-MM, S7 performs the best with the reduction in all the observed error statistics. In S4 and S5, all other error statistics are reduced except the minimum error. Comparing all three CA-MMs, the acceleration variation is the smallest in S7 as it is closer to a straight line, hence, performing the best. In CV-MM case, S9 is mostly satisfying the CV-MM assumptions and all the error statistics are reduced. The segments S6 and S10 performs the second best because of the good alignment with the straight-line assumption. In S11, on the other hand, the points are well aligned on a straight line but the velocity variance is quite high resulting in no improvement by the EKF framework. Finally, segments S3 and S8 are performing the worst by uplifting the error statistics due to the discontinuity in data points and misalignment from the straight line.

To sum up, even though the proposed EKF approach does not give the lowest errors in all circumstances, it reduces the highest error significantly for different types of motions model as long as the segment trajectory is in compliance with the MM assumption. It is also observed that the performance of the EKF depends on the noise covariance selection. Different noise covariances may improve errors at some particular points deteriorating at other points. One possible approach for this is to tune the EKF parameters at each state according to some prior knowledge. A reinforcement learning-based approach can be adopted in that case. The summary of this chapter is included in the Chapter 4.

Chapter 3

Localization with Deep Neural Networks using mmWave Ray Tracing Simulations

Research outcome

- **U. Bhattacherjee**, C. K. Anjinappa , L. Smith, E. Ozturk, and I. Guvenc, "Localization with Deep Neural Networks using mmWave Ray Tracing Simulations," in Proc. Southeastern Conf., Raleigh, NC, Mar. 12-15, 2020. [22]

3.1 Summary of the Chapter

The world is moving towards faster data transformation with more efficient localization of a user being the preliminary requirement. This chapter investigates the use of a deep learning technique for wireless localization, considering both millimeter-wave (mmWave) and sub-6 GHz frequencies. The capability of learning a new neural network model makes the localization process easier and faster. In this chapter, a Deep Neural Network (DNN) was used to localize User Equipment (UE) in two static scenarios. Two different methods are proposed to train a neural network, one using channel parameters (features) and another using a channel response vector, and compare their performances using preliminary computer simulations. It is observed that the former approach produces high localization accuracy: considering that all of the users have a fixed number of multipath components (MPCs), this method is reliant on the number of MPCs. On the other hand, the latter approach is independent of the MPCs, but it performs relatively poorly compared to the first approach.

3.2 Introduction

In the upcoming 5th generation (5G) wireless communication networks, one of the most promising enhancements will be larger data rates with increased coverage, which requires faster beamforming in a given direction to maintain uninterrupted communication. To accomplish this, a base station (BS) must know a user equipment's (UE) location within the network. The process of determining the location of a given UE within a particular area is called localization. Capability of localizing a UE can further be leveraged to provide location-based services by the cellular network. Thus, the process of localization is highly necessary in wireless communication.

In wireless networks, there exist many localization algorithms. In [23], the authors perform localization with the help of signaling data like Reference Signal Received Power (RSRP) and timing advance. In [24], authors compare different advanced algorithms, such as localization with hybrid Received Signal Strength (RSS) and Angle of Arrival (AOA), projection onto convex set, multi-hop methods, etc. In [25], the authors explore different Time-of-Arrival (TOA) based algorithms for localization. In general, these algorithms use channel parameters such as AOA, TOA, RSS as well as various channel statistics, derived from the channel parameters, to perform accurate localization. These procedures often involve time-consuming and complex operations, such as the least square methods mentioned in [24]. A geometry based perspective to improve localization performance using the non-line of sight (NLOS) paths is explored in [26, 27].

Researchers considered NLOS components as source of distortion in earlier studies [28]. However, the NLOS components increase the channel sparsity as few MPCs can be received with significant RSS, hence provide additional information about the location of a UE [29]. In [30], it is mathematically demonstrated that NLOS components are the most informative ones in case of narrow beams (e.g. mmWaves). The most popular features used to predict the location in the literature are AOA, TOA, and RSS. The authors in [31] provides the performance analysis of localization using these features. They observed different combinations of these features and found the result to be better for the combination of TOA and AOA, but not much reliable with RSS. The numerical analysis of these features using Monte-Carlo simulation can be found in [32].

The aforementioned works tackle the localization problem from a system modeling, signal processing, and even a geometry-based perspective. In this study, machine learning (ML) is leveraged to improve the localization process, in terms of low run-time complexity i.e. lower computation time without sacrificing the accuracy. The ML algorithms are capable of learning complicated functions if provided enough training samples. It is used extensively in the field of wireless communication for various tasks, such as the prediction of the Angle of Departure (AoD) channel feature from AOA [33], predicting channel characteristics of a massive multiple-input multiple-output (MIMO) system [34], classification of different types of Unmanned Aerial Vehicles (UAVs) [35], etc. ML is being used in localization research as well. In [36], the authors observe the effects of a BS or an eNodeB (eNB) on node localization. In this study, a deep neural network (DNN) is proposed to locate user nodes in a mmWave network. However to the best

of our knowledge, there is no study in the literature that compares mmWave and sub-6 GHz bands using ML techniques and explore the effect of using different channel parameters.

A supervised ML technique is used in this chapter and the localization problem is posed as a regression problem. In supervised learning, it is assumed that one has access to a set of learning features, measured over several observations, and an outcome variable (i.e.the UE location in this chapter), which is also known as the label or the target. The learning features can either be the combination of raw channel parameters, such as AOA, TOA, and RSS, or the channel response vector; see Section II for more details. The training data for the DNN was generated by Remcom's Wireless Insite, a ray-tracing simulator. Our preliminary results show that the proposed localization technique gives high accuracy considering a high signal-to-interference ratio (SNR) regime. Our future work includes studying the performance trade-offs in various different environments and SNRs, and exploring the effect of beam forming on the localization accuracy.

The rest of this chapter is organized as follows. Section 3.3 introduces the system model and problem formulation, including two different approaches for generating inputs for the DNN. Section 3.4 introduces the proposed DNN technique. Section 3.5 provides our preliminary simulation results.

3.3 System Model and Problem Formulation

This section describes how the channel features and location information provided by the ray-tracing model are transformed into input features and output labels for training a DNN at the BS side. In this process, two different approaches are mentioned that are followed in this chapter with relevant details.

As described briefly in Section 3.2, the training data for the DNN was obtained from ray-tracing simulations. The ray-tracing simulator generates channel parameters that capture the dependence of the environment geometry and transmitter/receiver locations, which are crucial for the ML applications. The choice of a dataset depends on our approach to designing the DNN, which is discussed up next.

3.3.1 Approach 1: Utilization of the Channel Parameters

This approach uses raw channel parameters observed at the BS, provided by the simulator i.e. AOA, TOA, and RSS, to train the DNN model in order to predict the location of the users. The number of inputs to the model depends on the selected number of MPCs and the number of features considered. For simplicity, the number of MPCs is fixed to three, and three different combinations of channel parameters are used to feed the model. Details of the DNN architecture for Approach 1 are as follows:

- **Input:** The number of inputs will vary for each combination of features - it will be the product of the number of MPCs and number of features.

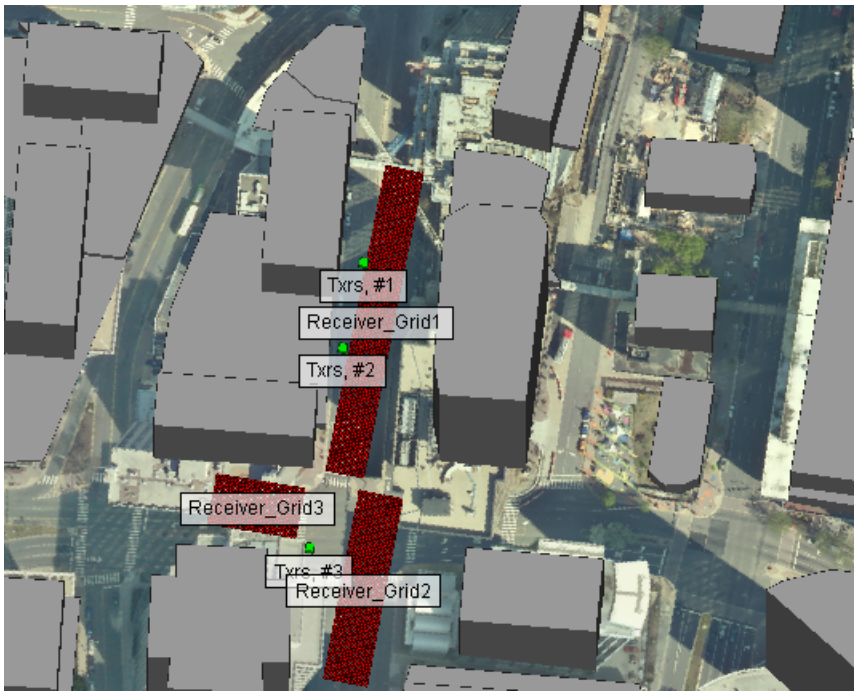

Figure 3.1 Approach 1: Ray tracing scenario in North Moore Street, Rosslyn, Virginia.

  - Only AOA (3 inputs)
  - Only AOA and RSS (6 inputs)
  - Only AOA, RSS and TOA (9 inputs)

- **Output:** The outputs to be observed are the x and y coordinates of a user's location. All the users are assumed to be on the same plane, thus the z coordinates are ignored.

Details of the trained DNN model are further discussed in Section III.

Intuitively, more MPCs will provide more information to the DNN to be trained more efficiently, but it will increase the training computational complexity and likelihood of overfitting as well. In this trade-off, three MPCs are considered to have the balance between accuracy and complexity.

Fig. 3.1 shows a scenario where a UE communicates with BSs. There are multiple UE grids (red path) and BS nodes (green point) within an urban environment. All of the nodes use half-wave dipole antennas at a height of 10 m from the ground and transmits at a power level of 0 dBm. They are excited with two different frequencies, 5 GHz and 28 GHz, with 100 MHz and 500 MHz bandwidths, respectively.

Specifically, for this study, *Txrs* #1 is the transmitter for which the channel parameters are observed for both receiver grid 2 and 3. All of the users in receiver grid 2 are in Line of Sight (LOS), and the users in receiver grid 3 are in Non-Line of Sight (NLOS). The UEs are spaced 1 meter apart from each other, and there are a total of 1530 receiver points, 990 in receiver grid

2, and 540 in receiver grid 3. The UE locations, within their respective receiver grid, serve as the expected output of the DNN.

Drawback of this approach: In this approach, we only consider a fixed number of MPCs which might not be a realistic assumption. This is because the actual number of MPCs vary in practice for each user due to the dynamic environment and scatterers. To make the model more flexible and independent of the number of MPCs, we took another approach, which is described below.

3.3.2 Approach 2: Utilization of the Channel Response Vector

In this approach, the channel response vector is considered as the input to the DNN model. Namely, the number of antennas is taken as inputs, which makes the system robust against the number of varying MPCs. For simplicity, a single antenna system is assumed on the UE and the number of antennas on the BS is set to 10. Details of the DNN architecture for Approach 2 is as follows:

- **Input:** The number of inputs will be the product of antennas at the BS and UE.
  - We pass the absolute value of the channel response vector as the input. The absolute value of the channel impulse response was calculated using functions provided in [37] [1].
- **Output:** As output the x and y coordinates of a user's location are considered. All the users are assumed to be on the same plane, thus the z coordinates are ignored.

In the scenario used here, UEs communicate with different BSs as shown in Fig. 3.2. The Deep-MIMO dataset was generated for ML researchers. For the DNN, BS3 is considered as the transmitter and the users (1000 - 1025 rows) from User grid 1 as receivers, which is 185 users in total. For each user, the channel response is generated as follows:

$$\mathbf{h}_k^{b,u} = \sum_{l=1}^{L} \sqrt{\frac{\rho_l}{K}} e^{j\left(\vartheta_l^{b,u} + \frac{2\pi k}{K}\tau_l^{b,u}B\right)} \mathbf{a}(\phi_{az}^{b,u}, \phi_{el}^{b,u}) \ , \tag{3.1}$$

where $h_k^{b,u}$ is the channel response vector at BS b from the UE u for subcarrier k. The $\rho_l, \vartheta_l, \tau_l, \phi_{az}, \phi_{el}$ are the RSS, Doppler frequency, TOA, AOA (azimuthal and elevation), respectively. The number of MPCs is denoted by L.

3.4 Deep Neural Network Preliminaries

In this section, we discuss some preliminaries and the overall architecture of the considered DNN.

[1] https://www.deepmimo.net/

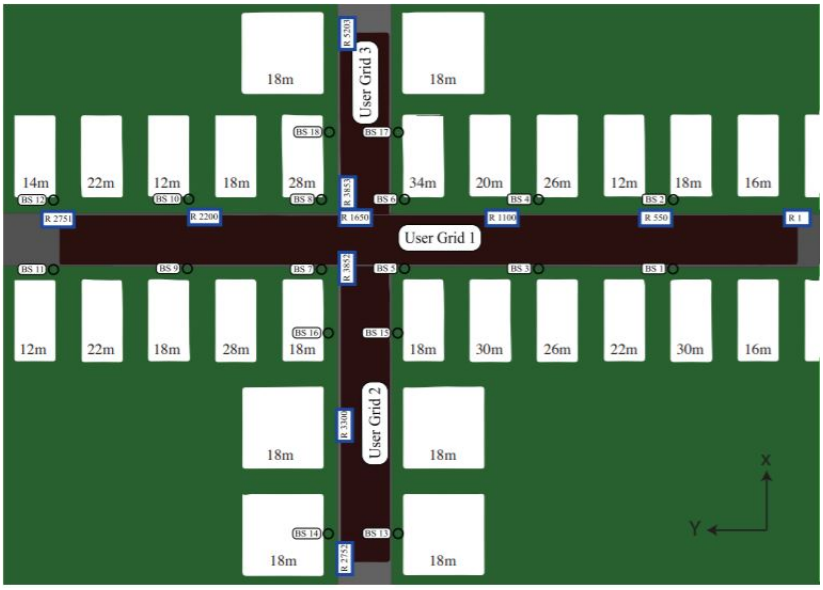

Figure 3.2 Approach 2: Ray tracing scenario from DeepMIMO dataset.

3.4.1 Input Features

As discussed earlier, the input features depend on the approach. For both approaches, the combination used as input is mentioned in Section 3.3 with appropriate normalization to the data set. An illustration of Approach 1 is shown in Fig. 3.3.

3.4.2 Output Labels

The Cartesian coordinates x and y of the location are considered as the output labels. The z coordinates are ignored since all the users are in same plane.

3.4.3 Hidden Layers and Hyper-parameters

Two hidden layers, as shown in the Fig. 3.3, are considered in this model. The other hyper-parameters, such as number of nodes in each hidden layer, learning rate and activation function, are optimized using the Bayesian optimization technique by calculating the mean square error (MSE). The grid of hyper-parameters used while training the DNN model are shown in Table 3.1.

Table 3.1 Hyper-parameters and their range.

	Range
Number of Nodes	4 to 50
Learning Rate	1e-3 to 1e-1
Activation Functions	tansig, logsig, purelin (linear), poslin (positive linear), radial basis (radbas)

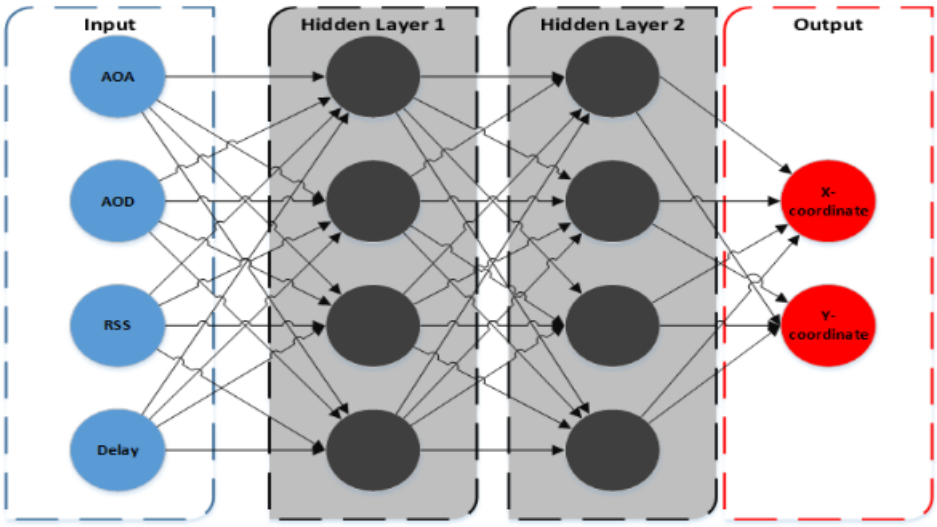

Figure 3.3 Illustration of DNN for approach 1.

3.4.4 Objective Function

The objective of a supervised learning process is to minimize a loss function. An example of a loss function is the binary cross-entropy in classification and the mean square error (or the quadratic loss) in regression type problems. In this chapter, the mean square error is considered as the loss function. The location is predicted as a learning-based optimization problem, as shown in (3.2). The goal of the optimization problem is to learn the mapping $\mathcal{F}$, such that the MSE between the known output and the estimated output is minimized:

$$\min_{\mathcal{F}} ||\mathcal{F}(\text{features}) - \text{output labels}||^2 \ . \tag{3.2}$$

The DNN model has been designed using MATLAB's deep learning toolbox. Given enough training data, the DNN can be trained well enough to learn complicated functions using the back-propagation algorithm.

3.5 Simulation Results

In this section, the simulation setup and the obtained results are discussed. For Approach 1, the localization problem is divided into two cases, LOS-based and NLOS-based localization. Apriori, it is known that all of the UEs in receiver grid 2 are in LOS and thus, possess a strong direct LOS signal component. Whereas, the UEs in receiver grid 3 are in NLOS. The total number of UEs for the LOS and NLOS cases are 990 and 540 user points, respectively. The simulations are performed at both 5 GHz and 28 GHz bands. For Approach 2, the considered region is located within the LOS area and has a total of 185 users.

For both approaches, the entire dataset is used for both training and testing purposes. The

Table 3.2 Frequency bands used in ray tracing simulations.

Frequency	Type of path	Inputs	Number of nodes in hidden layer 1	Number of nodes in hidden layer 2	Learning Rate	Activation Function
5 GHz	LOS	AOA	40	50	0.9078	logsig
		AOA + RSS	8	25	0.0010027	logsig
		AOA + RSS + TOA	4	50	0.0011179	tansig
	NLOS	AOA	40	38	0.40981	radbas
		AOA + RSS	42	50	0.1957	tansig
		AOA + RSS + TOA	29	31	0.93405	tansig
28 GHz	LOS	AOA	50	41	0.97691	tansig
		AOA + RSS	8	46	0.0012802	tansig
		AOA + RSS + TOA	15	46	0.8885	logsig
	NLOS	AOA	34	50	0.0010755	radbas
		AOA + RSS	9	50	0.9795	tansig
		AOA + RSS + TOA	35	35	0.32042	logsig

final hyper-parameters are obtained by performing Bayesian optimization. The trained model is used for testing the accuracy of proposed localization approaches. For Approach 1, location maps and the CDF plots are generated for two different frequencies. For Approach 2, only the location map is included. In the preliminary results in this chapter, a high-SNR regime is considered, the effects of noise is ignored for the sake of simplicity.

3.5.1 Bayesian Optimization Results

The optimization procedure starts with a random combination of predefined range of hyper-parameters given in Table 3.1. The function 'bayseopt' calculates the cost function and accordingly chooses the next combination. In this chapter, mean squared error is considered as the loss function and the the total cost is calculated adding up all loss values as (3.2). After trying 30 different combinations, it picks the best combination to train the actual DNN. Table 3.2 illustrates the best hyper-parameters obtained for different experiments. It is obvious from the table that the choice of hyper-parameters depends on the combination of input, scenarios, and frequency.

3.5.2 Approach 1 Results

Fig. 3.4 (a), (b), (c) give the location mappings for LOS users (Receiver grid 2) at 5 GHz. At this scenario, considering only AOA gives the worst results. When RSS is given as input along with AOA, the accuracy of the model increases significantly. Adding TOA with the previous two features improves the model but not as much as it does when RSS is added. This is because RSS and TOA are somewhat correlated. For a user far from the BS, TOA will be greater, and

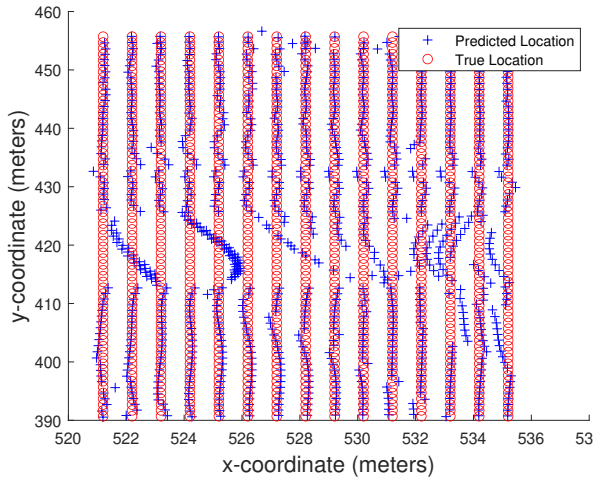

(a) Actual and predicted location using only AOA.

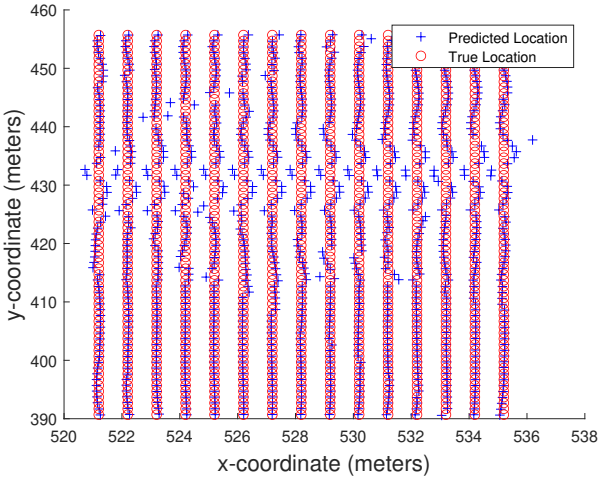

(b) Actual and predicted location using AOA and RSS.

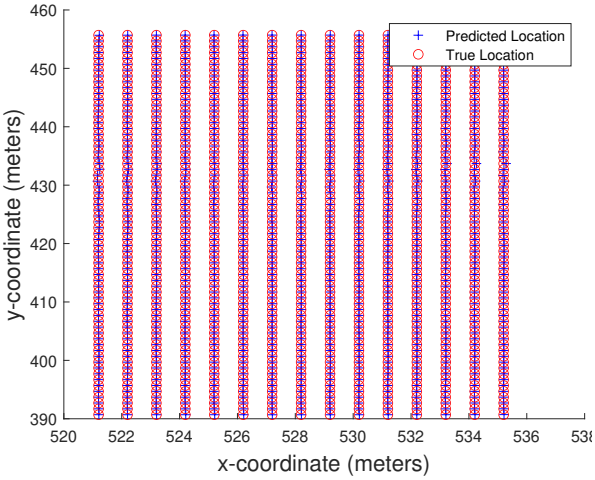

(c) Actual and predicted location using AOA, RSS and TOA.

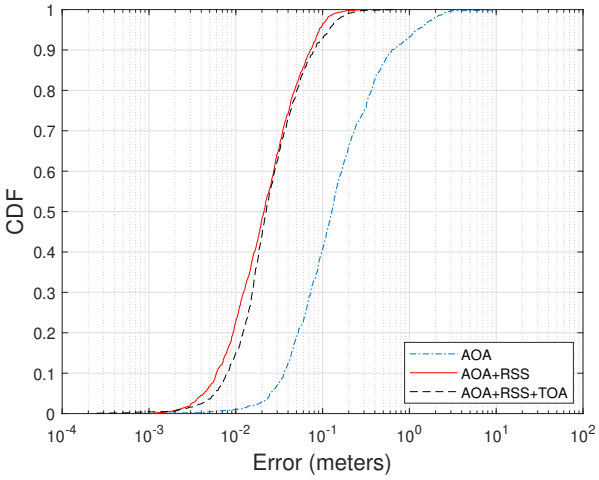

(d) CDF plot.

Figure 3.4 Location and CDF plot at 5 GHz (LOS).

RSS will be lower, and vice versa. Hence, in Fig. 3.4 (d), the CDF for AOA + RSS and AOA + RSS + TOA curves are almost overlapping. On the other hand, the error is less than 0.1 for 90% of the users, which is quite acceptable.

Fig. 3.5 (a), (b), (c) give the location mappings for NLOS users (receiver grid 3) at 5 GHz[2]. For NLOS case, the location mapping is not as accurate as it is for LOS scenario. In Fig. 3.5 (a), it can be observed that when only considering AOA, the error can be a maximum of 10 meters. However, as the number of features is increased i.e. adding RSS, and TOA, for 90% of the users, the error becomes less than 1 meter. For NLOS scenario at this frequency, the combination of

[2]Few predicted points that are outliers and significantly outside of the receiver grid have been ignored for the location maps for better visualization, but are included in the CDF plots.

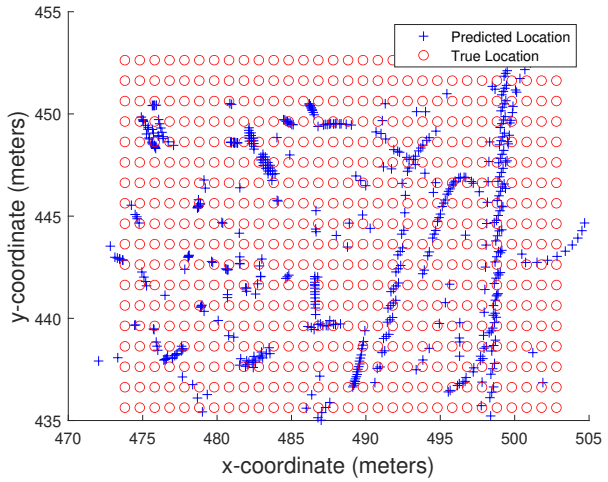

(a) Actual and predicted location using only AOA.

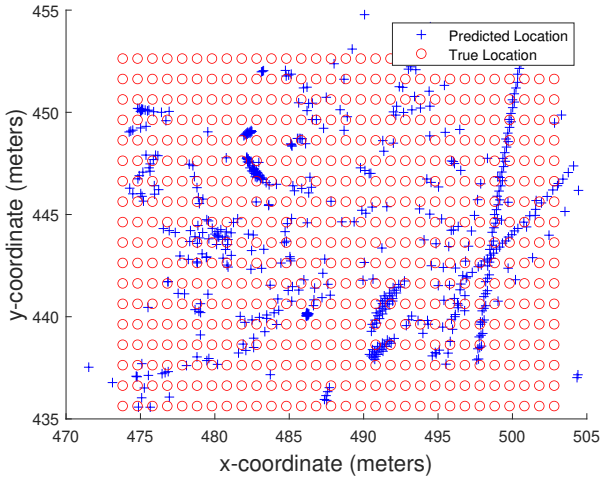

(b) Actual and predicted location using AOA and RSS.

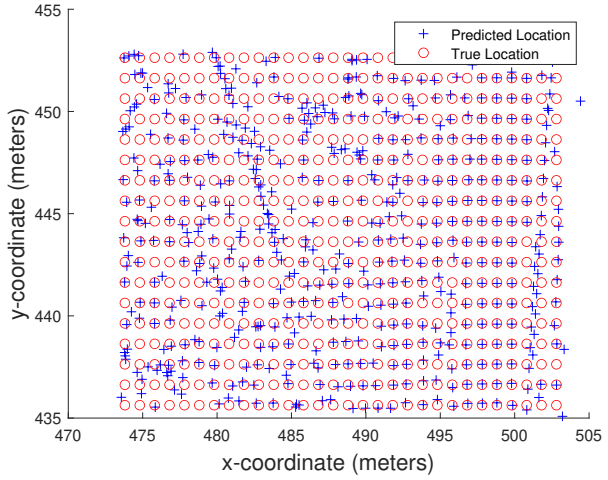

(c) Actual and predicted location using AOA, RSS and TOA.

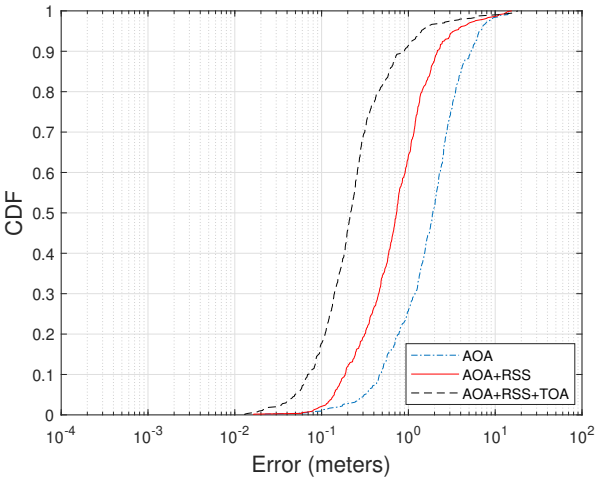

(d) CDF plot.

Figure 3.5 Location and CDF plot at 5 GHz (NLOS).

RSS, TOA, and AOA gives better results than the combination of RSS and AOA, since more than one MPCs are considered. Adding an extra degree of freedom improves the results.

Fig. 3.6 (a), (b), (c) give the LOS location mappings at 28 GHz. The trend of the results is similar to 5 GHz case. This time, adding TOA to the model as the third parameter does not increase the accuracy much. In Fig. 3.6 (d), the CDF plot shows that almost all users are having an error of less than 0.1 meter when all three channel parameters are used. As expected, in the case of NLOS users at this frequency, the results are not as good as the LOS case. The model gives the best estimations when all three parameters are considered. 90% of the users are having an error of less than 1 meter in that case.

Comparing the CDF curves for LOS and NLOS scenarios for both frequencies, it is observed that the curve is flatter in NLOS cases because the variation in error is higher. The performance

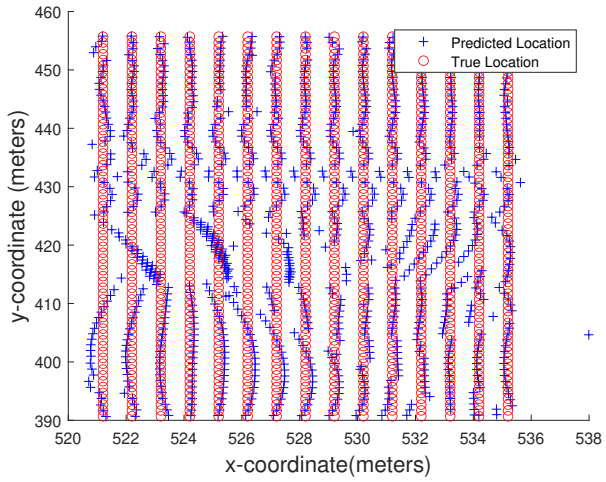

(a) Actual and predicted location using only AOA.

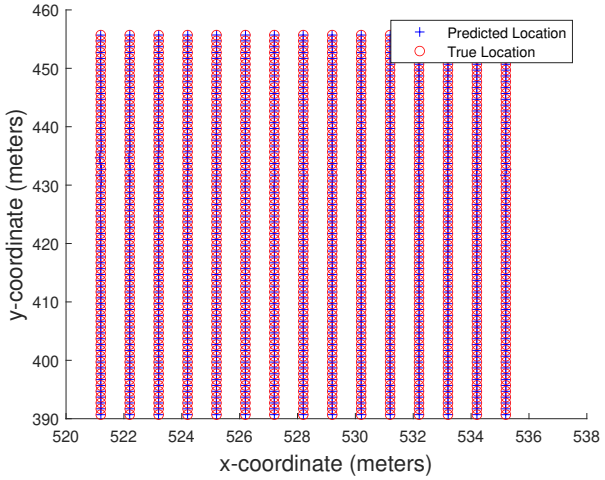

(b) Actual and predicted location using AOA and RSS.

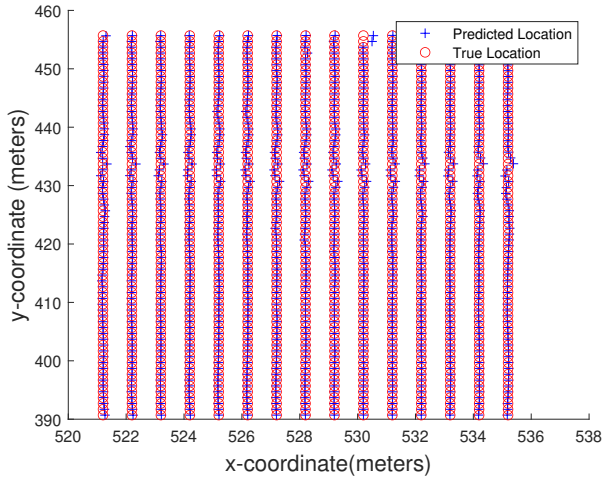

(c) Actual and predicted location using AOA, RSS and TOA.

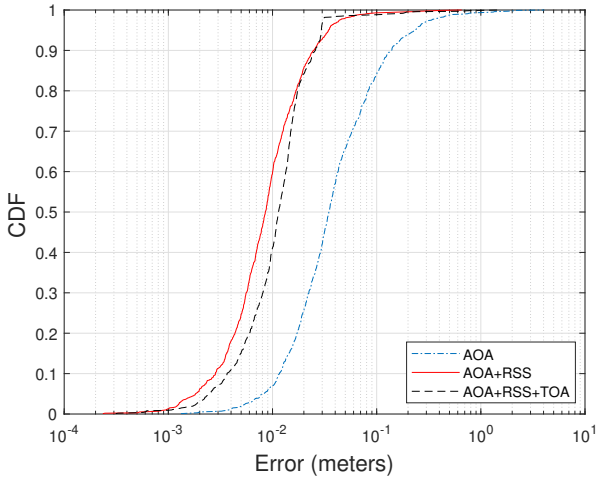

(d) CDF plot.

Figure 3.6 Location and CDF plot at 28 GHz (LOS).

of the DNN model towards NLOS points can be improved using more MPCs.

Comparing the results of 5 GHz and 28 GHz, one can observe the difference in the DNN performance. According to [38], it is expected to have a significant angular congruency between different frequency bands. In other words, the AOA and the AOD is expected to be close for the corresponding MPCs in two bands. Intuitively, both the 5 GHz and 28 GHz cases should yield similar results especially for the DNN based on AOAs only. However, our results do not align with this intuition.

One possible explanation for this could be the Bayesian optimization procedure, which starts the optimization with randomly chosen hyper-parameters that can be different in each training, even with the same inputs. As a result, the optimized final hyper-parameters can be

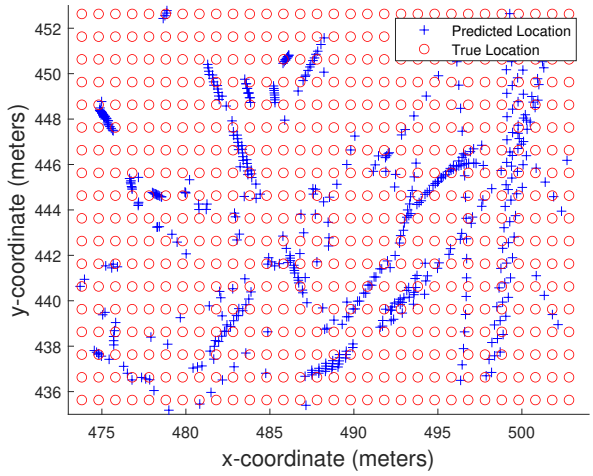

(a) Actual and predicted location using only AOA.

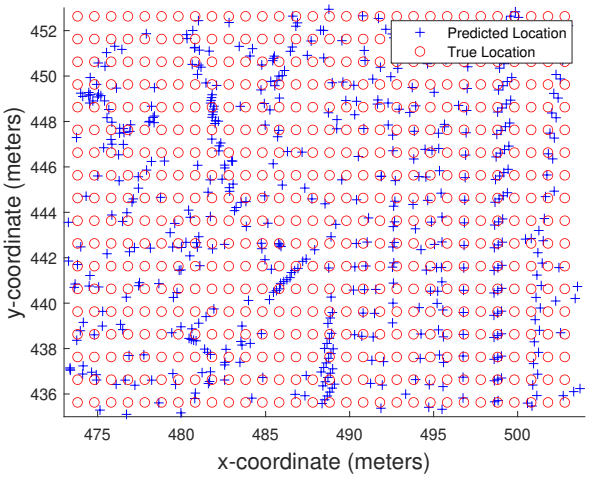

(b) Actual and predicted location using AOA and RSS.

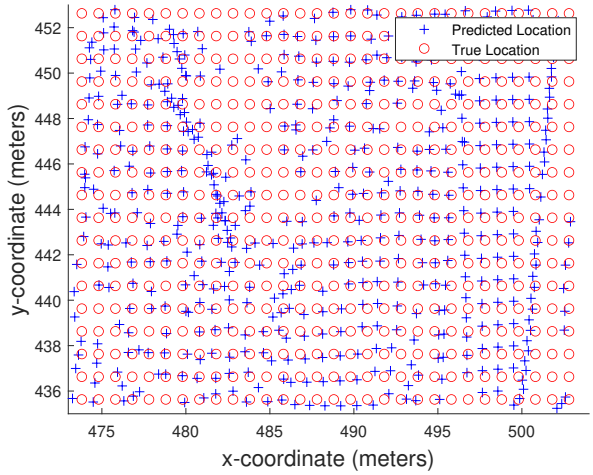

(c) Actual and predicted location using AOA, RSS and TOA.

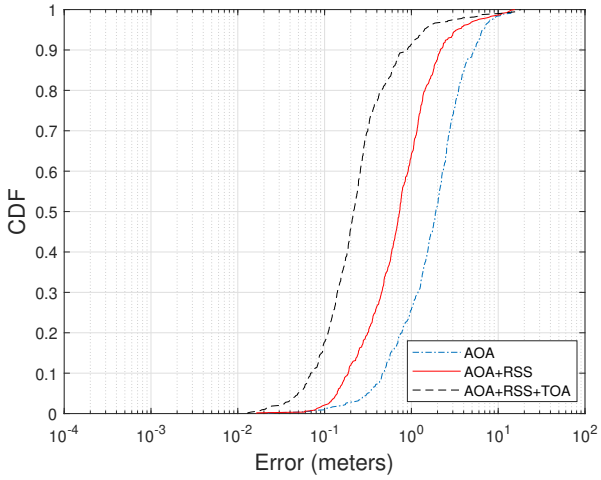

(d) CDF plot.

Figure 3.7 Location and CDF plot at 28 GHz (NLOS).

different. Second, the angular congruency may not hold at 5 GHz and 28 GHz. In the ray tracing simulations, the number of features is limited to 3, and these are based on the 3 most dominant MPCs arranged in descending order with respect to their powers. Thus, even though there exist significant angular congruency across the bands, the 3 chosen MPCs based on the dominant power might have mismatch in the AOAs. One explanation to this could be that, the diffraction gets less effective as the frequency increases, therefore it is more likely for a diffracted signal to be more powerful than reflected ones at 5 GHz band. It is also observed that 28 GHz frequency works better than sub-6 GHz band in NLOS scenarios and performance of the models do not differ much in LOS cases. This can be explained by the fact that the resolution of the model should be better with smaller wavelenghts, thus it is expected to have more accurate results at

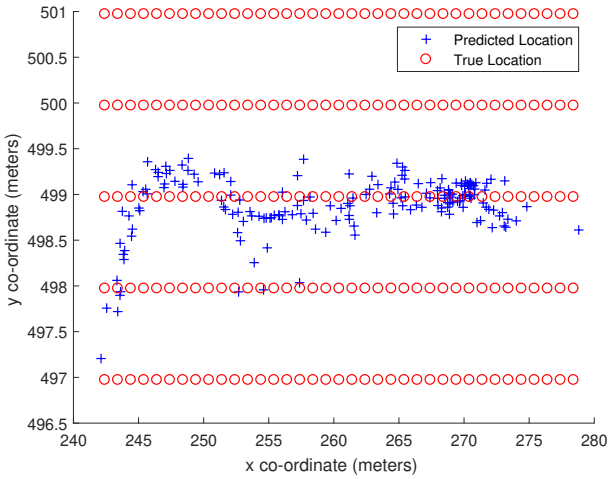

Figure 3.8 Actual and predicted locations for approach 2 Deep-MIMO dataset.

mmWave frequencies. However, in LOS cases, information provided by the existing features are representative enough to estimate the location of the UEs such that the difference in resolution cannot be observed.

3.5.3 Approach 2 Results

When the DNN is trained using a channel vector response, it cannot predict the location as expected (Fig. 3.8). The actual spacing between the users is about 1 meter. Since the users are closely located, there is not much difference in the channel response. Hence, the DNN fails to train itself properly. This problem can be solved by the feature transform technique used in [39]. Using this technique, the input features can be sparsely distributed so that the DNN can easily differentiate between two users, in terms of their channel response. The implementation of a feature transform is considered as a future work.

This chapter is concluded in the chapter 4.

Chapter 4

CONCLUSION

In the second chapter, penetration loss of several common constructional materials at 28 GHz, 39 GHz, 120 GHz, and 144 GHz were measured. The maximum distance from the Tx and the Rx to the materials was chosen to eliminate the edge scattering effect. The minimal distance from the Tx and the Rx to the materials was calculated to ensure both the Tx and the Rx antennas were in the far field region. Ground reflection was minimized by using narrow beam antennas. The measured constructional materials were ceiling tile, glass, drywall, and plywood. The penetration loss results, after being averaged over all the measured positions, ranged from 0.401 dB for ceiling tile at 28 GHz to 16.068 dB for plywood at 144 GHz. The highest attenuation of 27.633 dB/cm was observed for clear glass at 144 GHz. Overall, the penetration loss and attenuation increases with frequency for all the materials. These results could be helpful for developing mmWave and THz channel models that accurately estimate the penetration loss of common building materials. They can further contribute to link budget calculation for future 5G/6G deployments in indoor environments and for developing accurate penetration models for ray-tracing simulations.

The third chapter analyzed the propagation of 28 GHz mmWave signals based on the measurements conducted at Johnston Regional Airport. We compared the measurement results in indoor, outdoor, and indoor-to-outdoor scenarios with the theoretical propagation characteristics. The study showed that mmWave outdoor propagation had a higher path loss compared to indoor scenario. Indoor environment had rich scatterings and a wider signal coverage while received power in the outdoor airport environment was only dominated by a few rays. Moreover, mmWave had high FSPL and penetration loss, and hence it would be challenging to accomplish indoor-to-outdoor communication: the indoor-to-outdoor propagation therefore may need to be highly directional to recover the penetration loss through directionality gain. For both indoor and outdoor propagation, there were still a considerable number of reflected MPCs that had comparable received powers to the LOS MPC's received power, which may allow a feasible way to achieve mmWave NLOS communications during blockage of the dominant path(s), via the reflective objects in the channel environment. Our future work includes mmWave propagation measurements and analysis at larger airports and a wider range of communications frequencies.

BIBLIOGRAPHY

[1] H. Menouar, I. Guvenc, K. Akkaya, A. S. Uluagac, A. Kadri, and A. Tuncer, "UAV-enabled intelligent transportation systems for the smart city: Applications and challenges," *IEEE Communications Magazine*, vol. 55, no. 3, pp. 22–28, 2017.

[2] W. Kong, D. Zhou, Y. Zhang, D. Zhang, X. Wang, B. Zhao, C. Yan, L. Shen, and J. Zhang, "A ground-based optical system for autonomous landing of a fixed wing UAV," in *Proc. IEEE Int. Conf. on Intelligent Robots and Systems*, (Chicago, IL), pp. 4797–4804, Sep. 2014.

[3] I. Guvenc, F. Koohifar, S. Singh, M. L. Sichitiu, and D. Matolak, "Detection, tracking, and interdiction for amateur drones," *IEEE Commun. Magazine*, vol. 56, no. 4, pp. 75–81, 2018.

[4] C. Schüpbach, C. Patry, F. Maasdorp, U. Böniger, and P. Wellig, "Micro-UAV detection using DAB-based passive radar," in *Proc. IEEE Radar Conf.*, (Seattle, WA), pp. 1037–1040, May 2017.

[5] J. Klare, O. Biallawons, and D. Cerutti-Maori, "UAV detection with MIMO radar," in *Inter. Radar Symposium (IRS)*, (Prague), pp. 1–8, Jun 2017.

[6] J. Gong, J. Yan, D. Li, D. Kong, and H. Hu, "Interference of radar detection of drones by birds," *Progress In Electromagnetics Research*, vol. 81, pp. 1–11, 2019.

[7] P. Poitevin, M. Pelletier, and P. Lamontagne, "Challenges in detecting UAS with radar," in *Proc. IEEE Intern. Carnahan Conf. on Security Technology (ICCST)*, (Madrid), pp. 1–6, Oct. 2017.

[8] P. Nguyen, T. Kim, J. Miao, D. Hesselius, E. Kenneally, D. Massey, E. Frew, R. Han, and T. Vu, "Towards RF-based localization of a drone and its controller," in *Proc. IEEE Micro Aerial Veh. Netw. Syst. Appl.*, pp. 21–26, Jun. 2019.

[9] M. F. Al-Sa'd, A. Al-Ali, A. Mohamed, T. Khattab, and A. Erbad, "RF-based drone detection and identification using deep learning approaches: An initiative towards a large open source drone database," *Future Gen. Comp. Syst.*, vol. 100, pp. 86–97, 2019.

[10] "Keysight geolocation software." `https://www.keysight.com/us`.

[11] A. N. Mody, M. Sherman, A. Trojan, K. Yau, J. Farkas, S. Sputz, T. McElwain, R. Bauer, J. Boksiner, and A. Fiuza, "On making the current military radios cognitive without hardware or firmware modifications," in *Proc. IEEE Military Commun. Conf.*, (San Jose, CA), pp. 2327–2332, Nov. 2010.

[12] X. Liu, X. Liu, W. Zhang, and Y. Yang, "Interacting multiple model UAV navigation algorithm based on a robust cubature kalman filter," *IEEE Access*, vol. 8, pp. 81034–81044, 2020.

[13] V. Marojevic, I. Guvenc, M. Sichitiu, and R. Dutta, "An experimental research platform architecture for UAS communications and networking," in *Proc. IEEE Veh. Tech. Conf. (VTC)*, (Honolulu, HI), pp. 1–5, Sep. 2019.

[14] J. Lategahn, M. Muller, and C. Rohrig, "TDoA and RSS based extended Kalman filter for indoor person localization," in *Proc. IEEE Veh. Tech. Conf. (VTC)*, (Las Vegas, NV), pp. 1–5, Sep. 2013.

[15] X. R. Li and V. P. Jilkov, "Survey of maneuvering target tracking: dynamic models," in *Signal and Data Processing of Small Targets 2000*, vol. 4048, pp. 212–235, Int. Soc. for Optics and Photonics, 2000.

[16] D. Laneuville, "Polar versus cartesian velocity models for maneuvering target tracking with IMM," in *Proc. IEEE Aerospace Conf.*, pp. 1–15, 2013.

[17] K. Mehrotra and P. R. Mahapatra, "A jerk model for tracking highly maneuvering targets," *IEEE Trans. Aerospace and Electronic Syst.*, vol. 33, no. 4, pp. 1094–1105, 1997.

[18] S. P. Linder and C. Schell, "A non-bayesian segmenting tracker for highly maneuvering targets," *IEEE Trans. Aerospace and Electronic Syst.*, vol. 41, no. 4, pp. 1168–1177, 2005.

[19] E. Çintaş, B. Özyer, and E. Şimşek, "Vision-based moving UAV tracking by another UAV on low-cost hardware and a new ground control station," *IEEE Access*, vol. 8, pp. 194601–194611, 2020.

[20] F. Govaers, *Introduction and Implementations of the Kalman Filter*. BoD–Books on Demand, 2019.

[21] G. Zhai, H. Meng, and X. Wang, "A constant speed changing rate and constant turn rate model for maneuvering target tracking," *Sensors*, vol. 14, no. 3, pp. 5239–5253, 2014.

[22] U. Bhattacherjee, C. K. Anjinappa, L. Smith, E. Ozturk, and I. Guvenc, "Localization with deep neural networks using mmwave ray tracing simulations," in *Proc. IEEE SoutheastCon 2020*, pp. 1–8, 2020.

[23] L. Ni, Y. Wang, H. Tang, Z. Yin, and Y. Shen, "Accurate localization using LTE signaling data," in *Proc. IEEE Int. Conf. on Computer and Info. Tech. (CIT)*, (Helsinki, Finland), pp. 268–273, 2017.

[24] A. Coluccia and A. Fascista, "A review of advanced localization techniques for crowdsensing wireless sensor networks," *Sensors*, vol. 19, p. 988, Feb. 2019.

[25] I. Guvenc and C.-C. Chong, "A survey on TOA based wireless localization and NLOS mitigation techniques," *IEEE Commun. Surveys & Tutorials*, vol. 11, pp. 107–124, Aug. 2009.

[26] M. Ruble and I. Güvenç, "Wireless localization for mmWave networks in urban environments," *EURASIP Journal on Advances in Sign. Proc.*, vol. 2018, p. 35, Dec. 2018.

[27] M. C. Ruble, "Massive MIMO millimeter wave channel estimation and localization." PhD Dissertation, NC State University, 2018.

[28] N. Garcia, H. Wymeersch, E. G. Larsson, A. M. Haimovich, and M. Coulon, "Direct localization for massive mimo," *IEEE Trans. on Signal Proc.*, vol. 65, pp. 2475–2487, May 2017.

[29] Hua Deng and A. Sayeed, "Mm-wave MIMO channel modeling and user localization using sparse beamspace signatures," in *Proc. IEEE Int. Workshop on Sig. Proc. Adv. in Wireless Commun. (SPAWC)*, (Toronto, ON, Canada), pp. 130–134, Jun. 2014.

[30] R. Mendrzik, H. Wymeersch, G. Bauch, and Z. Abu-Shaban, "Harnessing NLOS components for position and orientation estimation in 5G millimeter wave MIMO," vol. 18, pp. 93–107, Jan. 2019.

[31] F. Lemic, J. Martin, C. Yarp, D. Chan, V. Handziski, R. Brodersen, G. Fettweis, A. Wolisz, and J. Wawrzynek, "Localization as a feature of mmWave communication," in *Proc. Int. Wireless Commun. and Mobile Comp. Conf. (IWCMC)*, (Paphos, Cyprus), pp. 1033–1038, Sep. 2016.

[32] H. El-Sayed, G. Athanasiou, and C. Fischione, "Evaluation of localization methods in millimeter-wave wireless systems," in *Proc. IEEE Int. Workshop on Computer Aided Modeling and Design of Commun. Links and Networks (CAMAD)*, (Athens, Greece), pp. 345–349, Dec. 2014.

[33] S. Navabi, C. Wang, O. Y. Bursalioglu, and H. Papadopoulos, "Predicting wireless channel features using neural networks," in *Proc. IEEE Int. Conf. Commun. (ICC)*, (Kansas City, MO), pp. 1–6, IEEE, 2018.

[34] L. Bai, C.-X. Wang, J. Huang, Q. Xu, Y. Yang, G. Goussetis, J. Sun, and W. Zhang, "Predicting wireless mmWave massive MIMO channel characteristics using machine learning algorithms," *Wireless Commun. and Mobile Computing*, vol. 2018, 2018.

[35] M. Ezuma, F. Erden, C. K. Anjinappa, O. Ozdemir, and I. Guvenc, "Micro-UAV detection and classification from RF fingerprints using machine learning techniques," in *Proc. IEEE Aerospace Conf.*, (Big Sky, MT), pp. 1–13, 2019.

[36] M. Z. Comiter, M. B. Crouse, and H. Kung, "A data-driven approach to localization for high frequency wireless mobile networks," in *Proc. IEEE Global Commun. Conf. (GLOBECOM)*, (Singapore), pp. 1–7, 2017.

[37] A. Alkhateeb, "DeepMIMO: A generic deep learning dataset for millimeter wave and massive MIMO applications," *arXiv preprint arXiv:1902.06435*, 2019.

[38] C. K. Anjinappa and I. Guvenc, "Angular and temporal correlation of V2X channels across sub-6 GHz and mmWave bands," in *Proc. IEEE Int. Conf. Commun. (ICC) Workshops*, (Kansas City, MO), pp. 1–6, May 2018.

[39] C. Studer, S. Medjkouh, E. Gönültaş, T. Goldstein, and O. Tirkkonen, "Channel charting: Locating users within the radio environment using channel state information," *IEEE Access*, vol. 6, pp. 47682–47698, Jul. 2018.